Geophysical Journal International

Geophys. J. Int. (2011) **184,** 1009–1022 doi: 10.1111/j.1365-246X.2010.04912.x

Present-day crustal deformation along the Magallanes–Fagnano Fault System in Tierra del Fuego from repeated GPS observations

L. Mendoza,[1,2] R. Perdomo,[1,2] J. L. Hormaechea,[1,2,3] D. Del Cogliano,[1,2] M. Fritsche,[4] A. Richter[4] and R. Dietrich[4]

[1] *Universidad Nacional de La Plata, Facultad de Ciencias Astronómicas y Geofísicas, Departamento de Astrometría, Paseo del Bosque s/n,* B1900FWA *La Plata, Argentina. E-mail: lmendoza@fcaglp.unlp.edu.ar*
[2] *CONICET, Argentina*
[3] *Estación Astronómica Río Grande, Acceso Aeropuerto,* V9420EAR *Río Grande, Argentina*
[4] *Technische Universität Dresden, Institut für Planetare Geodäsie,* 01062 *Dresden, Germany*

Accepted 2010 November 30. Received 2010 November 30; in original form 2010 April 6

SUMMARY

The present-day deformation of the earth crust in the Argentine part of Tierra del Fuego main island (southernmost South America) is here investigated based on repeated geodetic GPS observations. The island is traversed by the active transform boundary between the South American and Scotia tectonic plates, represented by the Magallanes-Fagnano fault system. Since 1993 a regional network comprising to date 29 GPS sites has been observed almost every year. The complete set of accumulated observations was processed using the Bernese GPS software and state-of-the-art processing strategies and models. The utilization of homogeneous GPS products resulting from a reprocessing of the global IGS network warrants a stable realization of a global reference frame. For each GPS site 3-D positions and linear velocities with error estimates were obtained. A strain analysis of the horizontal velocity components revealed the zones of major deformation activity. A 30-km-wide deformation belt centred on the main trace of the fault system was identified. This belt is bordered to the north (South America) and south (Scotia) by geodynamically stable zones, which move horizontally with a relative average velocity of 4.4 ± 0.6 (east) and -0.3 ± 0.4 (north) mm a^{-1}. Within the deformation belt a maximum strain rate in the order of 0.25 μstrain per year has been detected. A pronounced change in the deformation style from transtension (east) to transpression (west) is observed. The area of predominating shortening of the crust coincides with a local rotation minimum and relative uplift. Throughout the period covered by the GPS observations the displacements and deformations occurred to be linear with time.

Key words: Satellite geodesy; Transform faults; Neotectonics; South America.

1 INTRODUCTION

Tierra del Fuego (TDF), southernmost South America, is of particular geodynamic and tectonic interest. The region is traversed by the recently active transform boundary between the South America (SA) and Scotia (SC) tectonic plates (Pelayo & Wiens 1989). It is the only place where a boundary of SC Plate rises above the sea and thus presents a unique opportunity to directly observe the movement in connection with the geodynamic processes occurring along its length. In this work, we investigate the present-day horizontal crustal deformations in the Argentine part of TDF main island based on repeated geodetic Global Positioning System (GPS) measurements.

Geologically, the island is divided into three structural zones (from NE to SW): the Magallanes basin, the Magallanes fold and thrust belt, and the Fuegian Andes (Olivero & Martinioni 2001; Menichetti *et al.* 2008); the latter representing the southernmost segment of the Andean Cordillera. The present-day tectonic setting is primarily controlled by the Magallanes–Fagnano Fault System (MFFS, Lodolo *et al.* 2003). According to geological, geomorphological and geophysical results, the MFFS is characterized by a left-lateral strike-slip regime. It represents the present-day SA–SC tectonic plate boundary in this region and accommodates their relative movements (Pelayo & Wiens 1989; Lodolo *et al.* 2003). Geological evidence for strike-slip movements in nowadays TDF dates back to 30 Ma (Olivero & Martinioni 2001), when the onset of seafloor spreading in the SC Sea which lead to the opening of the Drake Passage and the separation of Antarctica from SA (Cunningham *et al.* 1995; Barker 2001). The MFFS may have gained its predominant role in accommodating the relative SA–SC movements around 7 Ma, after cessation of seafloor spreading in the western SC Sea (Lodolo *et al.* 2003). The distribution of Cretaceous-Eocene units in the eastern part of the island suggests a left-lateral offset of the

order of 20–30 km since the latest Eocene (Olivero & Martinioni 2001).

The MFFS extends from the Atlantic offshore to the western arm of the Strait of Magellan and splits the TDF main island into two continental blocks. Running in E–W direction through the southern part of the island it manifests its geomorphological expression in a series of lineaments and depressions. From the Atlantic coast just south of Cape Malengüena it follows the valleys of Irigoyen River, Turbio River and Fagnano Lake (Lodolo *et al.* 2003; Menichetti *et al.* 2008). The main trace of the MFFS leaves the 105 km long Fagnano Lake in its western part across the northern shore. However, in this area, as well as near the Atlantic coast, where the main trace is frequently offset and cut by N–S trending faults, the limited geological, geomorphological and geophysical data still fail to provide unambiguous constraints for the exact location of the active faults and the partitioning of the strike-slip motions (Lodolo *et al.* 2003; Tassone *et al.* 2005; Menichetti *et al.* 2008). To the north and south, the main trace of the MFFS is accompanied by a number of sub-parallel secondary faults, the most important ones being the Deseado, the Carbajal Valley and the Beagle Channel Faults (Menichetti *et al.* 2008).

The recent activity of the MFFS is also revealed by the seismicity in the region. Compared to other continental plate boundaries, the seismicity in TDF is described as relatively low (Lodolo *et al.* 2003). Nevertheless, the historical earthquake records include two events on 1949 December 17 of magnitude 7.5 and 7.8 (epicentres 69.0° W 54.2° S and 69.7° W 53.9° S, respectively) (Jaschek *et al.* 1982), a magnitude 7.0 event in 1879 (Lomnitz 1970), and several earthquakes of magnitude >6 during 1930 and 1944 (Jaschek *et al.* 1982). The records of the International Seismological Centre indicate nearly 30 moderate (magnitude $\sim$5) earthquakes in the region between 1960 and 1997 (Willemann & Storchak 2001). Since 1999 the Facultad de Ciencias Astronómicas y Geofísicas, Universidad Nacional de La Plata (FCAG-UNLP, Argentina) and the Instituto Nazionale di Oceanografia e di Geofisica Sperimentale (OGS, Italy) have installed and operated a seismological network in the Argentine part of TDF which to date comprises four stations. Since then, more than 300 low magnitude earthquakes spatially related with the MFFS have been recorded (Buffoni *et al.* 2009). The average magnitude is below 2, but several magnitude three to four events were perceived by the inhabitants in Tolhuin and Ushuaia over the last 10 years. On 2009 November 6, a magnitude 5.2 earthquake occurred (epicentre 70.6° W 54.0° S according to preliminary analysis results).

Precise Global Navigation Satellite Systems (GNSS, including GPS) positioning constitutes a powerful technique to observe crustal deformation processes both on global (e.g. Drewes 2009) and regional (e.g. Dietrich *et al.* 2009) scales. In TDF geodetic GPS observations commenced in 1993. The first direct determination of the relative movement across the MFFS, $\sim$5 mm a^{-1}, was obtained by Del Cogliano *et al.* (2000) based on GPS observations spanning seven years. Smalley *et al.* (2003) obtained a relative velocity of 6.6 ± 1.3 mm a^{-1} on the basis of an independent set of GPS observations and assuming a vertical strike-slip fault model with 15 km locking depth. Both papers did not resolve transpression nor transtension for the region under investigation.

Here we present a regional geokinematic investigation of the Argentine part of TDF main island. Our observation data include those used by Del Cogliano *et al.* (2000) but are greatly extended in time and densified in space. The accuracy of the determined site velocities benefits, on one hand, from the accumulation of 14 episodic GPS campaigns (during a time span of 16 years), and on the other hand, from the application of a consistent global reference frame and homogeneous products resulting from a reprocessing of the International GNSS Service (IGS) network (Steigenberger *et al.* 2006; Rülke *et al.* 2008). We apply the tool of strain analysis to the obtained horizontal velocity components in order to describe and interpret the presently active crustal deformations in the region.

2 GPS DATA PROCESSING

2.1 GPS data set

The GPS observation time series used in this work include data from 29 regional sites shown in Fig. 1 (28 campaign sites plus one IGS permanent tracking station operative since 1997). These sites were repeatedly observed during several campaigns in the period 1993–2008. Most of the campaigns were performed in the summer season and elapsed several days to more than a month, with observation sessions spanning some hours to weeks.

The earliest observations (before 2003) were performed by researchers from FCAG-UNLP and from Estación Astronómica Río Grande (EARG). Since 2003 up to the present, this project, including the field work, has been carried out jointly by the former institutes with researchers from Institut für Planetare Geodäsie, Technische Universität Dresden (IPG-TUD). In Table 1 all the GPS campaigns performed in the TDF region are listed, detailing each site occupation's time, and the mounting system used for the antenna setup (i.e. tripod or forced centring). Table 1 shows also the relative contribution of each campaign, in cumulative observation time, with respect to the total data set.

For the regional observations only L1 and L2-capable GPS receivers were used, including Ashtech Z–XII, Trimble 4000 and Trimble 4700 models. In order to minimize systematic effects, usually one and the same individual antenna was utilized during the occupations of a given site. However this was not always possible, especially during the early campaigns. In order to account for antenna changes on the sites as well for the diversity of utilized antenna models an antenna field calibration was performed.

The regional data set was completed with observations from nine IGS sites (shown in Fig. 1, inset), for the purpose of connecting the network to the global reference frame. Considering the location of the region under investigation, IGS sites on the South American and Antarctic continents as well as on islands in the Pacific and Atlantic oceans were chosen.

2.2 Processing scheme

The GPS observation analysis was performed using the *GPS Bernese Software 5.0*. The raw GPS data was arranged in 183 daily sessions, including all the available observations from the regional and IGS sites shown in Fig. 1.

In a first step, each defined session was processed independently, involving code smoothing, receiver clock synchronization, baseline definition, phase screening for outliers rejection and integer ambiguity resolution. Daily normal equations (NEQs) were formed based on double-difference phase observations. The correlations between double-difference observations, including inter-baseline correlations, were treated in a mathematical rigorous manner. All defined parameters but the site positions (e.g. site-specific tropospheric delays, remaining ambiguities) were pre-eliminated from each NEQ. The position parameters of regional sites which were

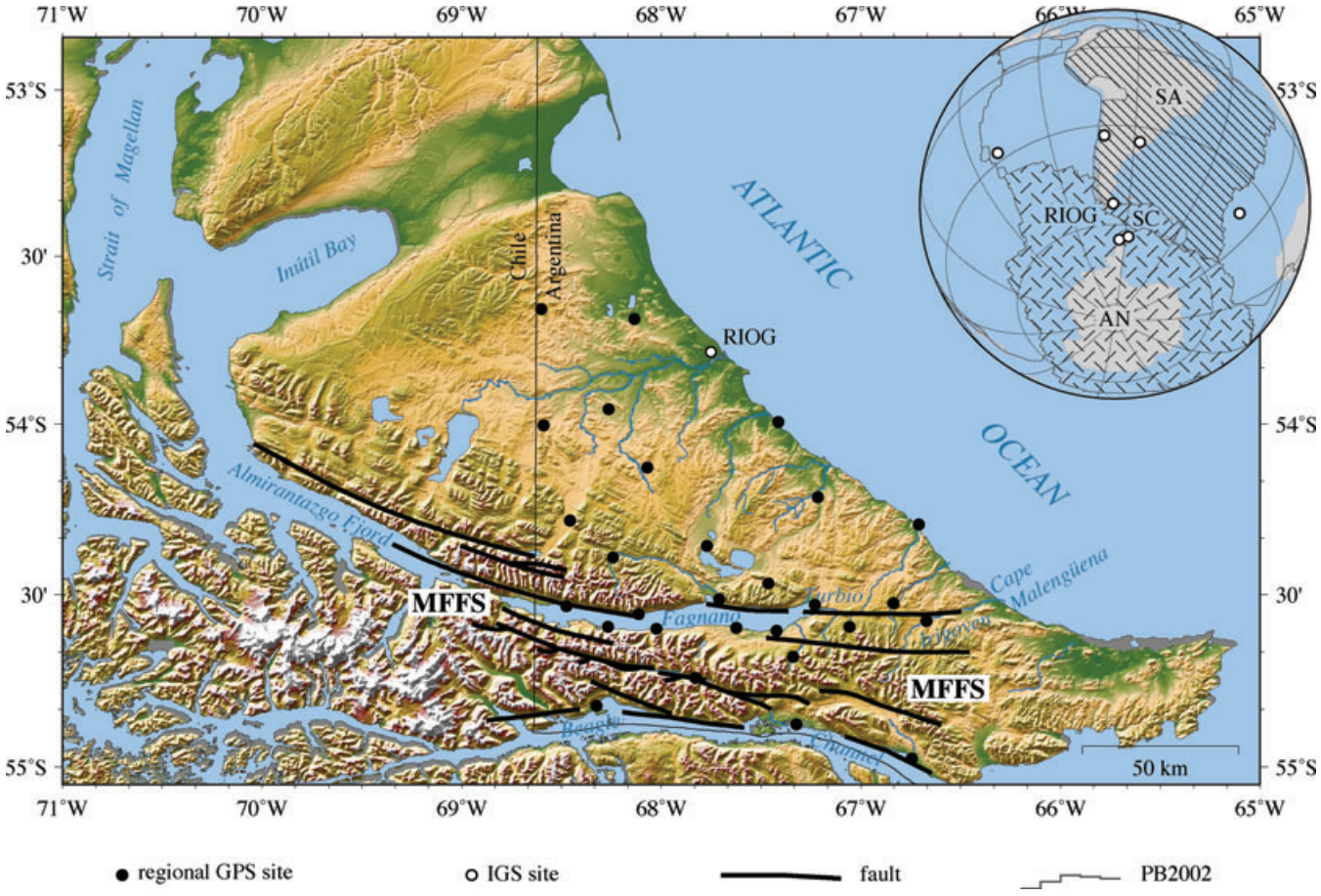

Figure 1. Map of the TDF main island showing the 28 GPS sites included in the regional network. The identified main faults associated to the MFSS, adapted from Menichetti *et al.* (2008), are plotted superimposed to the topography of the island (SRTM, Rodríguez *et al.* 2005). The inset shows the included IGS permanent tracking stations and the SA, SC and Antarctic (AN) tectonic plates boundaries, taken from the model PB2002 (Bird 2003).

observed in less than three campaigns were also pre-eliminated to avoid an ill-conditioned or singular cumulative system.

In a second step, the resulting NEQs were stacked and for each GPS site a set of 3-D positions (at a reference epoch $t_0 = 2000$) and constant velocity components was parametrized. In addition, six pseudo-observations were added to the resulting cumulative NEQ to introduce a no net translation (NNT) condition between a priori and estimated positions and velocities of six IGS sites. By means of these minimum constraints strategy the datum of the estimated regional frame was defined. To define the NNT condition, *a priori* values from the IGS05 (Ferland 2006) reference frame were used.

2.3 Products and models

We have not used standard products of the IGS but an alternative set of required products, which was generated in a self-consistent way, and which is homogeneous throughout the time span of the regional GPS campaigns. These products, described by Steigenberger *et al.* (2006) and known as Potsdam–Dresden Reprocessing products (PDR), include precise satellite orbits, Earth orientation parameters (EOP), global ionospheric maps and differential code biases (DCB). Further information about these products can be found in Steigenberger *et al.* (2008) and Rülke *et al.* (2008).

A field calibration of receivers antenna phase centre offsets and variations (PCO and PCV) was carried out, in order to account for the utilization of different antennas on a specific site. Systematic effects associated with instrumentation changes on the sites may induce errors of several centimetres on the estimated parameters (Rothacher *et al.* 1995), which propagate directly to the vertical components of positions and velocities and to the estimated tropospheric delays.

Instrument-dependent PCO and PCV were estimated using the same GPS Bernese Software 5.0 (Beutler *et al.* 2007) version as for the regional network data processing. Due to the observing and processing strategies the resulting models are consistent with the TUM05 (Schmid *et al.* 2007) models for satellite and receiver antennas (see Table 2). Although not all the antennas involved in the regional campaigns were available to perform the calibration—some antennas were decommissioned years before—the estimated instrument-specific models account for 91.4 per cent of the total regional GPS observation data. Additional models involved in the data analysis are listed in Table 2.

2.4 Campaign's position repeatability

In order to quantify the position repeatability for each yearly observation campaign partial adjustments were performed including only data from that specific year and estimating site positions for the mean campaign epoch. Positions and velocities, taken from the cumulative solution described in Section 2.2, were used to compute a priori values for the position parameters of the regional sites; these *a priori* values were also used, before inverting each campaign's

Table 1. List describing the regional GPS data set used in the analysis. For each site, the accumulated hours of observation during each campaign and the method of antenna mounting (tripod or forced centring) are shown. Campaigns indicated with † represent the data subset used by Del Cogliano *et al.* (2000). The percentages in the bottom indicate the contribution, in accumulated time of observation, from each campaign to the grand total.

	1993†	1994†	1995†	1997†	1999†	2000	2001	2002	2003	2004	2005	2006	2007	2008
CADI	10	8	6	9	21	9	8	20	20	16	162	56	·	·
DESP	17	7	7	26	8	9	·	·	9		24	·	·	46
EOLO	18	14	27	26	21	23	4	16	24	63	58	25	106	46
ESCO	·	·	·	·	·	·	·	·	·	91	40	35	·	51
ESPE	·	·	·	·	·	·	·	·	75	149	79	102	·	·
ESSA	·	·	·	·	·	·	·	·	·	84	59	81	101	39
EUSH	·	·	·	·	·	·	·	·	104	131	119	54	·	·
FLAM	9	·	·	·	·	7	·	·	·	·	26	·	·	115
GUAZ	12	9	7	26	7	17	4	·	·	·	49	·	·	·
HARB	·	·	·	28	9	15	·	14	53	75	74	71	·	·
IRIS	·	·	·	·	·	·	·	·	·	·	148	·	184	142
KOSO	·	·	·	·	·	·	·	·	35	99	69	·	·	73
MOAT	6	8	8	8	6	9	·	25	19	39	95	41	·	·
ORJA	·	·	·	·	·	·	·	·	24	64	21	·	·	39
PALA	·	·	·	·	·	·	·	·	75	74	78	71	·	·
PISA	·	·	·	·	·	·	·	·	69	68	74	·	·	·
PJUS	14	10	16	26	11	18	8	8	24	26	85	·	·	·
PRE2	·	·	·	·	·	·	·	·	116	177	127	53	·	35
RADM	5	·	·	·	·	8	·	·	·	·	25	·	·	68
RHAM	16	8	15	27	13	22	4	14	89	48	109	93	·	·
RIOC	10	9	·	·	·	23	38	·	59	26	176	42	·	·
RIOG	·	·	·	IGS	IGS	IGS	IGS	IGS	IGS	IGS	IGS	IGS	IGS	IGS
RIOS	·	·	·	·	·	·	·	·	31	92	166	98	·	·
SALV	7	·	·	·	·	·	·	·	·	·	55	·	·	184
SPAB	8	6	6	26	6	11	·	14	27	49	38	·	119	95
TERM	·	·	·	·	·	8	·	·	127	160	328	179	257	413
TORI	·	·	·	·	·	·	·	·	71	109	71	98	·	·
VIAM	8	7	9	26	12	5	4	·	·	·	63	·	·	73
YEHU	14	13	11	31	15	17	·	·	54	97	56	·	·	·
	1.9 per cent	1.0 per cent	1.2 per cent	2.3 per cent	1.2 per cent	1.7 per cent	0.6 per cent	1.2 per cent	9.6 per cent	15.2 per cent	24.8 per cent	10.5 per cent	11.2 per cent	17.6 per cent

tripod forced centring

Table 2. Summary of products and models involved in the GPS observations analysis.

Product/model	Brief description
Orbits	From PDR (Steigenberger *et al.* 2006), extended until 2008
EOP	From PDR (Steigenberger *et al.* 2006), extended until 2008
Satellite's PCO & PCV	SV-specific z-offset, block-specific x- & y-offsets, absolute nadir-dependent variations, from TUM05 (Schmid *et al.* 2007)
Receiver's PCO & PCV	Absolute elevation- & azimuth-dependent variations and offsets, from TUM05 (Schmid *et al.* 2007) plus instrument-specific models (see Section 2.3)
DCB	From PDR (Steigenberger *et al.* 2006), extended until 2008
Ionosphere	From PDR (Steigenberger *et al.* 2006), L_3 linear combination; second- & third-order effects considered (Fritsche *et al.* 2005)
Troposphere	*A priori*: hydrostatic troposphere delay mapped with IMF; estimated: one zenith delay each 2 hours, mapped with wet NMF
Solid Earth tides	IERS Conventions 2003, McCarthy, D. and Petit, G. (eds), 2004, step 1 and step 2, 'Conventional Tide Free' crust
Ocean loading	FES2004, www.oso.chalmers.se/∼loading/

NEQ, to introduce an NNT condition on these sites. Therefore, the campaign solutions were obtained in the same reference frame as the cumulative solution.

The rms derived from the residuals of each campaign solution with respect to the cumulative solution are shown in Table 3. The daily average interval of observation, the angular elevation mask and the percentage of antennas with tripod and forced centring antennas are also printed for each campaign. With the increase of the average observation interval and the number of forced centring antennas a clear reduction of the rms is observed. This behaviour is also related to the lower elevation mask of observation used in the later campaigns (after 2003).

Table 3. The rms of the positions' residuals, computed for each campaign solution w.r.t. the cumulative solution, are shown (regional sites only). The daily average interval of observation, the angular elevation mask and the percentage ratio tripod/forced centring antennas are indicated for each campaign.

	East (mm)	North (mm)	Up (mm)	$\overline{\Delta t}$ (h)	$\angle$ (°)	T/F (per cent/per cent)
1993	7	6	23	3	10	82/18
1994	8	15	16	4	10	78/22
1995	3	3	13	4	10	71/29
1997	6	6	23	13	10	76/24
1999	6	7	24	4	10	60/40
2000	2	4	18	5	10	73/27
2001	4	5	8	7	10	83/17
2002	2	4	12	7	10	55/45
2003	1	3	7	16	3[a]	25/75
2004	1	2	4	16	3[a]	22/78
2005	2	2	6	17	3	35/65
2006	2	2	4	16	3	12/84
2007	<1	1	2	22	3	0/100
2008	<1	1	2	19	3	31/69

[a]A few observations using a 15° angular elevation mask were also included in these campaigns.

Longer observation intervals and lower elevation masks allow a better modelling of site specific phenomena (e.g. local tropospheric delays). These phenomena affect mainly the estimation of the vertical component. Observations from lower elevations allow to better decouple the local tropospheric zenith delays from the estimated vertical site coordinate, while longer observations provide also a higher number of ambiguities resolved as integers. Forced centring antennas avoid two error sources: the intrinsic mechanical instability of the tripods (affected by wind, thermal dilatation, etc.) and possible installation eccentricities. The slightly larger N–S component of the horizontal rms is explained by the 'southern hole', a region of the southern sky were GPS satellites are never visible (Rothacher *et al.* 1995).

2.5 Site position repeatability

As for the campaign solutions, daily solutions were computed by inverting each session's NEQ. A similar approach, as for the campaign case, was used to set up a priori positions for the regional sites and to introduce a NNT constraint for the datum definition. The purpose of these adjustments is twofold: (1) to detect, and to treat accordingly, any position outliers, mainly due to installation eccentricities and (2) to confirm the implicit hypothesis of linearity of the movements for the regional sites. Fig. 2 shows the obtained residuals, for each daily solution with respect to the cumulative solution, for two representative sites, one observed repeatedly with tripod and the other observed with forced centring antenna. The position repeatability of those sites observed with forced centring antennas results at least two times smaller than the corresponding for those sites observed with tripods.

A few position outliers were detected, mainly related to misplaced tripods or incorrect instrumental heights, and the corresponding daily observations from these sites were preeliminated from the cumulative system before inverting the NEQ. For none of the sites the daily residuals reveal any indication of non-linearity of the observed motions.

2.6 Error assessment of the site velocities

It is well known that the formal errors of the estimated site velocities (σ, *a posteriori* standard deviation, see Table 4) are too optimistic. These overoptimistic results are commonly encountered when estimating parameters from GPS observations and they are mainly due to two reasons: (1) commonly, and in order to simplify the computations, it is assumed that the observations are uncorrelated (white noise model) and (2) the adjustment is performed over a huge number of observations (e.g. ionosphere-free linear combinations), resulting in a very large number of degrees of freedom, which leads to very small standard deviations for the estimated parameters. For the reasons given above it is a common practice to derive standard deviations for site velocities from the time series residual position. In addition, in order to obtain more realistic uncertainties which take into account the correlation of the observations with time, a power noise model (coloured noise) can be used. This assumption introduces a scaling of the error measure by a factor 2–5 (Zhang *et al.*

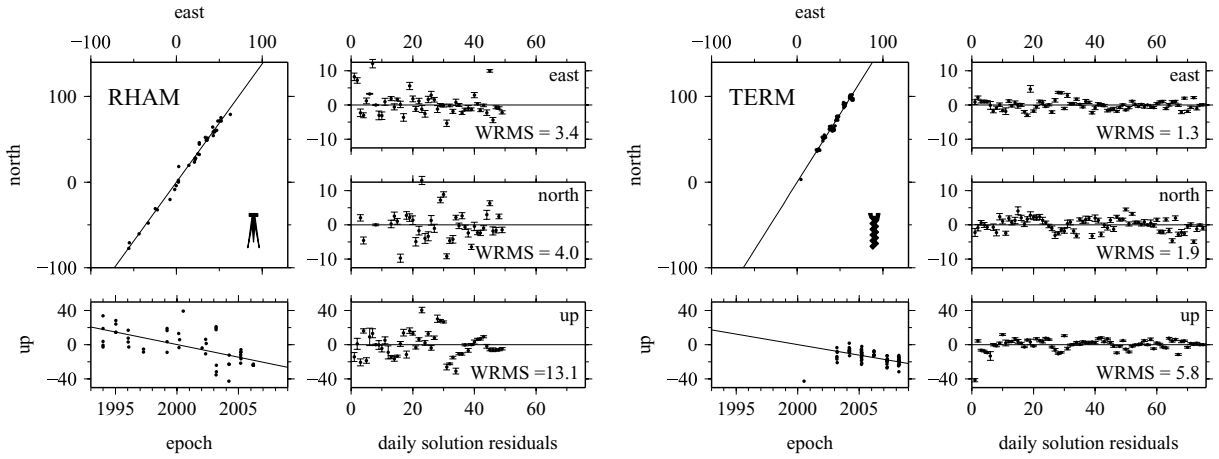

Figure 2. Daily positions w.r.t. the cumulative solution for two representative regional sites: RHAM, observed with tripod and TERM, with antenna mounted directly on bedrock (see Fig. 3 for site locations). All residuals in millimetres; straight lines represent the cumulative solutions; *a posteriori* formal error bars (2σ, 95 per cent confidence) for each daily solution residual included; weighted rms for each component are given. A vertical outlier detected for the site TERM is probably due to a misreported antenna adapter.

Table 4. Topocentric velocities estimated for each regional site with formal errors (2σ, 95 per cent confidence) and correlations ρ.

	Latitude (°)	Longitude (°)	v_e (mm a^{-1})	v_n (mm a^{-1})	v_{up} (mm a^{-1})	$\rho_{v_e v_n}$	$\rho_{v_e v_{up}}$	$\rho_{v_n v_{up}}$
CADI	54.823 S	68.324 W	8.09 ± 0.04	11.14 ± 0.04	−3.08 ± 0.18	−0.08	0.03	0.14
DESP	53.955 S	68.265 W	3.29 0.03	12.18 0.03	−3.53 0.13	−0.11	0.04	0.14
EOLO	54.528 S	67.231 W	4.84 0.03	12.17 0.03	−0.05 0.09	−0.16	0.04	0.14
ESCO	54.593 S	67.058 W	5.99 0.04	12.02 0.04	0.02 0.18	−0.06	0.01	0.05
ESPE	54.556 S	68.113 W	6.55 ± 0.05	12.42 ± 0.06	1.03 ± 0.24	−0.04	0.00	0.09
ESSA	54.523 S	66.838 W	4.99 0.04	12.60 0.04	−1.34 0.19	−0.07	0.00	0.09
EUSH	54.466 S	67.464 W	5.01 0.05	12.69 0.06	0.64 0.28	−0.01	0.00	0.05
FLAM	53.687 S	68.134 W	4.12 0.04	13.52 0.05	−4.25 0.19	−0.02	0.05	0.10
GUAZ	54.126 S	68.071 W	3.72 ± 0.04	12.14 ± 0.04	−2.27 ± 0.15	−0.09	0.03	0.12
HARB	54.876 S	67.324 W	8.10 0.03	12.04 0.04	−0.07 0.14	−0.10	0.02	0.09
IRIS	54.575 S	66.672 W	5.34 0.04	11.54 0.04	0.27 0.15	−0.07	0.01	0.06
KOSO	54.604 S	67.423 W	6.19 0.04	12.74 0.04	3.72 0.19	−0.06	0.01	0.05
MOAT	54.975 S	66.745 W	8.08 ± 0.04	12.92 ± 0.04	−3.25 ± 0.16	−0.09	0.06	0.09
ORJA	54.282 S	68.457 W	4.63 0.04	13.09 0.05	−0.52 0.20	−0.05	0.01	0.04
PALA	54.599 S	68.024 W	6.37 0.05	13.38 0.07	3.05 0.30	−0.02	0.01	0.03
PISA	54.533 S	68.475 W	7.12 0.06	9.67 0.09	4.61 0.35	−0.01	0.00	0.05
PJUS	54.213 S	67.216 W	2.97 ± 0.03	11.93 ± 0.04	−2.22 ± 0.14	−0.11	0.01	0.09
PRE2	54.595 S	67.625 W	6.87 0.04	11.58 0.04	1.69 0.17	−0.08	0.01	0.05
RADM	54.003 S	68.590 W	3.44 0.04	12.65 0.05	−1.01 0.20	−0.06	0.00	0.12
RHAM	54.741 S	67.829 W	8.66 0.03	11.96 0.03	−2.94 0.13	−0.12	0.04	0.13
RIOC	54.390 S	68.242 W	4.37 ± 0.04	13.33 ± 0.04	1.60 ± 0.17	−0.08	0.02	0.12
RIOG	53.785 S	67.751 W	3.46 0.03	12.09 0.02	2.37 0.07	−0.21	0.07	0.16
RIOS	4.512 S	67.710 W	4.09 0.05	11.87 0.07	0.11 0.26	−0.01	0.01	0.03
SALV	53.658 S	68.602 W	3.66 0.04	12.13 0.05	−4.57 0.19	−0.04	0.03	0.08
SPAB	54.293 S	66.710 W	3.03 ± 0.03	11.73 ± 0.03	−1.81 ± 0.11	−0.15	0.03	0.12
TERM	54.680 S	67.340 W	7.75 0.03	12.32 0.03	−2.46 0.10	−0.16	0.03	0.13
TORI	54.593 S	68.268 W	6.69 0.05	12.27 0.06	4.50 0.27	−0.03	0.00	0.00
VIAM	53.993 S	67.414 W	2.56 0.03	13.20 0.03	−4.71 0.12	−0.15	0.02	0.12
YEHU	54.356 S	67.772 W	3.78 ± 0.03	12.20 ± 0.04	−4.72 ± 0.14	−0.12	0.02	0.10

1997; Williams 2003), depending on the length of the time-series (i.e. the number of daily solutions).

In this analysis the following scheme was used to estimate more realistic errors: from the time series residual position of each site (e.g. Fig. 2) error estimates for each component of the velocities were computed, taking into account both the number of daily solutions and its time span; then, the error estimates were scaled by a factor of 3, common to all sites, accounting for the fact that coloured noise is present in the time series (Williams 2003). Due to the differences on the method of antenna mounting (tripod or forced centring), the number of daily solutions and the time span, the realistic uncertainties of the horizontal velocities vary between

0.1 (sites RIOG, TERM, IRIS) and 1.6 mm a^{-1} (site FLAM), while the realistic uncertainties for the vertical velocities vary between 0.4 (sites RIOG, TERM, IRIS) and 2.0 mm a^{-1} (sites PJUS, DESP).

The realistic errors estimated in this way represent the uncertainty of the absolute velocities in the global frame (IGS05). On the other hand, it is known that moving from global to regional solutions there exists a reduction in time-correlated noise within the regional network, due to the spatial correlation of the noise (Williams *et al.* 2004). For this reason, and because the subsequent deformation analysis will rely only on differential velocities between neighbourhood sites, the full variance–covariance matrix of the site velocities containing the formal uncertainties were introduced into the strain analysis.

2.7 Regional velocity field

The availability of a very long regional observation time series, together with a high quality, consistent and homogeneous set of required products and the use of state-of-the-art software and processing strategies, have resulted in a reliable, highly precise and dense reference frame for the TDF region.

The topocentric velocity components associated to the regional frame are listed in Table 4, including their formal errors and correlations; the horizontal components are plotted in Fig. 3. This discrete velocity field reveals that the TDF region can be roughly differentiated into two zones, to the north and south of the parallel 54.6° S which coincides approximately with the basin of the Fagnano Lake. While the average magnitude of the horizontal velocities in both zones are similar, ∼1.3 cm a^{-1}, the presence of a differential displacement becomes evident from a significant change in the direction of the movements. The limit between the two zones, inferred from the present geodetic results, is in perfect agreement with the identified faults that compose the MFFS (Menichetti *et al.* 2008). Consequently, the regional frame, and particularly its associated horizontal velocities, constitutes a well-suited basis to study the present-day relative crustal deformation in the region under investigation.

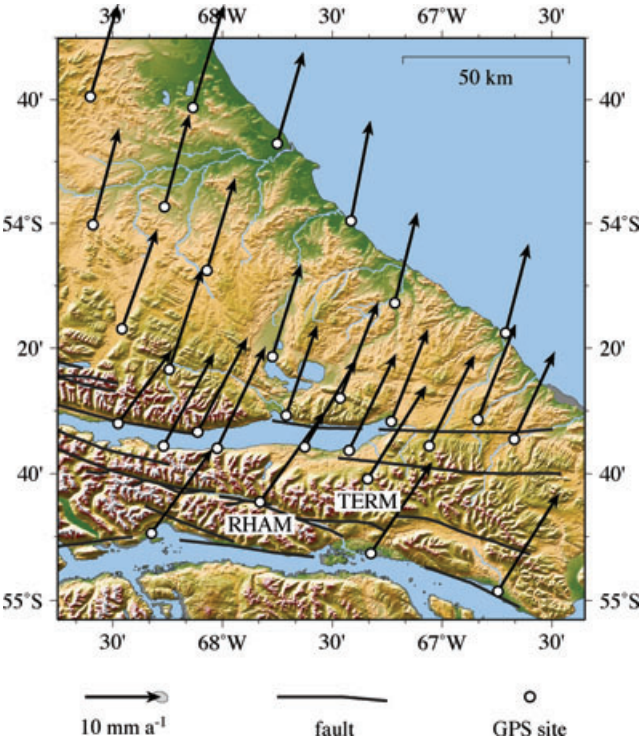

Figure 3. Observed horizontal velocity components. The velocities, originally obtained in a geocentric frame, were transformed to local topocentric systems (the formal error ellipses are not visible due to the scale of the velocity vectors).

3 GEOKINEMATIC INTERPRETATION

3.1 Deformation modelling

In order to quantify the present-day horizontal deformations in TDF, and under the assumption of stationary and homogeneous deformation rates on (small) finite areas, a detailed strain analysis on the obtained regional velocity field was performed. The parameters resulting from this analysis are invariant with respect to any of the constraints introduced for the geodetic datum realization, and constitute unbiased estimates for the regional strain rate (Bibby 1982).

The horizontal velocities of the 29 regional GPS sites (28 regional plus RIOG) were associated to displacements per unit of time, leading to deformation rate parameters. In parallel, the full variance–covariance matrix of the velocities, including intersite correlations, were formally propagated to the calculated quantities, resulting in significant correlations and confidence intervals for the deformation parameters.

For this analysis modified versions of the expressions given by Pietrantonio & Riguzzi (2004) were implemented. Our main modifications consist in: (1) an adaptation of the parametrization to horizontal deformation rate to prevent the propagation of vertical errors to the horizontal deformation parameters; (2) the simultaneous computation of a rigid rotation rate, which otherwise could contaminate the computed strain rate parameters and (3) the

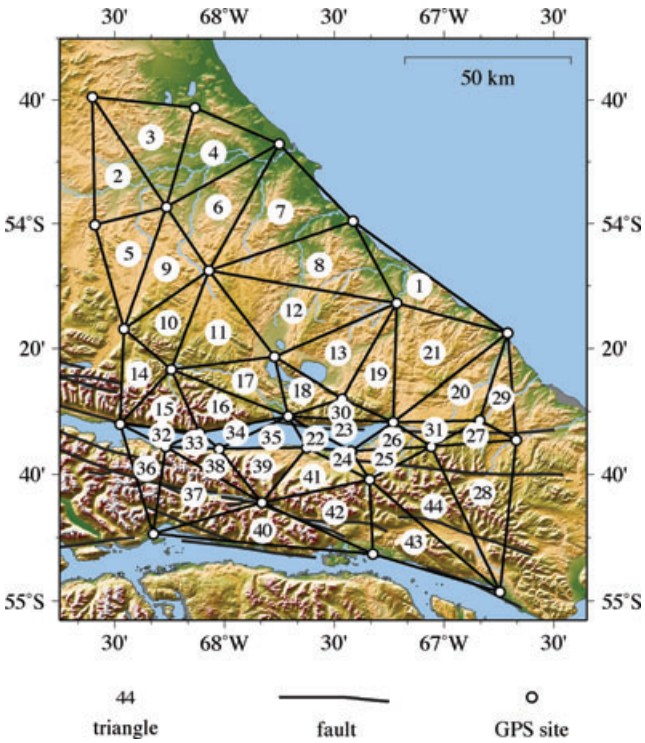

Figure 4. Subdivision of the GPS network into 44 triangles for each of which the horizontal velocities of the vertex were transformed to deformation rate parameters. The location of the faults was considered in the configuration.

Table 5. Absolute average displacement rates, rigid rotation rates and strain rate principal components, for each triangle, including their formal errors (2σ, 95 per cent confidence) and formal correlations ρ between the strain rate principal components.

Tri.	$\overline{v}_e$ (mm a^{-1})	$\overline{v}_n$ (mm a^{-1})	ω (mas a^{-1})	λ_1 (μstrain a^{-1})	λ_2 (μstrain a^{-1})	α_1 °(NESW)	$\rho_{\lambda_1\lambda_2}$	$\rho_{\lambda_1\alpha_1}$	$\rho_{\lambda_2\alpha_1}$
1	2.85 ± 0.02	12.29 ± 0.02	2.7 ± 0.2	−0.001 ± 0.001	0.057 ± 0.002	85.2 ± 1.1	0.06	0.60	0.72
2	3.46 0.02	12.32 0.03	−2.5 0.2	−0.018 0.002	−0.003 0.001	29.3 4.0	−0.09	−0.04	−0.12
3	3.69 0.02	12.61 0.03	2.5 0.2	−0.011 0.001	0.060 0.002	130.6 0.7	−0.06	−0.14	−0.07
4	3.63 0.02	12.60 0.02	−6.7 0.2	−0.010 0.001	0.054 0.002	88.9 0.7	−0.06	−0.44	−0.36
5	3.78 ± 0.02	12.64 ± 0.03	2.0 ± 0.3	−0.038 ± 0.001	0.023 ± 0.002	33.4 ± 1.2	−0.04	−0.04	0.22
6	3.49 0.02	12.14 0.02	1.1 0.2	−0.004 0.001	0.019 0.001	24.3 2.4	0.17	0.66	0.46
7	3.24 0.02	12.48 0.02	2.1 0.1	−0.044 0.001	−0.003 0.001	128.3 0.8	0.00	−0.24	−0.21
8	3.08 0.02	12.43 0.02	3.2 0.1	−0.017 0.001	0.056 0.001	81.7 0.5	0.03	0.26	0.24
9	3.87 ± 0.02	12.47 ± 0.02	0.5 ± 0.3	−0.044 ± 0.001	0.016 ± 0.002	42.8 ± 1.0	−0.17	−0.18	−0.02
10	4.24 0.02	12.85 0.03	−0.3 0.3	−0.044 0.001	−0.016 0.003	34.6 3.2	−0.03	0.03	0.29
11	3.95 0.02	12.55 0.02	−1.9 0.2	−0.047 0.001	0.004 0.001	37.7 1.0	−0.01	0.28	0.26
12	3.49 0.02	12.09 0.02	1.0 0.1	−0.021 0.001	0.001 0.001	55.1 2.4	0.23	0.63	0.65
13	3.92 ± 0.02	12.27 ± 0.03	8.8 ± 0.3	−0.051 ± 0.002	0.036 ± 0.002	29.4 ± 1.1	0.24	0.77	0.61
14	5.38 0.03	12.03 0.04	21.0 0.5	−0.090 0.003	0.119 0.003	94.5 0.6	−0.02	0.08	0.22
15	6.01 0.03	11.81 0.04	27.2 0.5	−0.036 0.003	0.108 0.003	88.5 0.9	0.01	0.14	0.20
16	5.00 0.03	12.54 0.03	12.4 0.4	−0.116 0.003	0.088 0.003	59.8 0.7	0.24	0.59	0.69
17	4.08 ± 0.03	12.47 ± 0.03	−1.8 ± 0.3	−0.035 ± 0.002	0.031 ± 0.003	55.4 ± 1.8	0.28	0.73	0.69
18	4.30 0.03	12.25 0.03	4.6 0.5	0.020 0.003	0.070 0.004	156.1 3.3	0.15	−0.55	−0.47
19	4.27 0.02	12.26 0.03	1.5 0.4	−0.067 0.003	0.028 0.002	53.3 0.9	−0.32	−0.30	−0.59
20	4.28 0.02	12.17 0.02	9.9 0.2	−0.055 0.001	0.026 0.002	25.5 1.0	0.27	0.85	0.57
21	3.61 ± 0.02	11.94 ± 0.02	4.6 ± 0.1	−0.039 ± 0.000	0.022 ± 0.001	46.5 ± 0.5	0.04	0.23	0.35
22	5.72 0.03	12.06 0.03	45.5 0.8	−0.145 0.006	0.156 0.006	61.5 0.9	0.26	0.66	0.75
23	5.04 0.02	12.26 0.03	19.0 0.4	−0.128 0.004	0.070 0.003	31.3 0.8	0.25	0.70	0.69
24	6.94 0.02	12.22 0.02	33.5 0.7	−0.089 0.005	0.133 0.006	71.6 1.1	0.22	0.64	0.82
25	6.64 ± 0.02	12.36 ± 0.02	15.6 ± 0.4	−0.093 ± 0.002	0.126 ± 0.003	48.1 ± 0.6	0.17	0.54	0.52
26	5.67 0.02	12.31 0.02	13.3 0.4	−0.106 0.003	0.085 0.003	40.9 0.7	0.20	0.59	0.58
27	5.44 0.02	12.05 0.03	6.6 0.5	−0.039 0.002	0.152 0.006	69.5 0.9	0.16	0.61	0.48
28	6.47 0.02	12.17 0.02	4.3 0.2	−0.063 0.001	0.015 0.001	41.0 0.6	−0.20	−0.16	−0.18
29	4.45 ± 0.02	11.96 ± 0.02	−2.7 ± 0.5	−0.091 ± 0.003	0.084 ± 0.003	45.5 ± 0.5	−0.33	−0.48	−0.41
30	4.65 0.03	12.24 0.03	−7.6 0.8	0.006 0.003	0.135 0.010	116.6 2.1	0.24	−0.82	−0.58
31	5.27 0.02	12.26 0.02	16.6 0.4	−0.039 0.003	0.097 0.004	52.3 1.2	0.30	0.76	0.73
32	6.79 0.03	11.46 0.05	7.8 1.0	−0.212 0.013	−0.003 0.004	163.6 1.6	0.17	−0.54	−0.69
33	6.54 ± 0.03	12.69 ± 0.04	5.2 ± 1.1	−0.133 ± 0.014	−0.004 ± 0.004	161.6 ± 2.8	0.14	−0.48	−0.56
34	5.67 0.03	12.56 0.04	7.5 1.0	−0.189 0.012	−0.074 0.004	12.8 2.8	0.15	0.62	0.73
35	5.77 0.03	12.28 0.03	22.1 0.6	−0.170 0.005	0.188 0.004	42.1 0.6	0.27	0.70	0.70
36	7.30 0.03	11.04 0.04	25.5 0.8	−0.102 0.005	0.066 0.004	123.2 1.0	−0.29	0.19	0.56
37	7.81 ± 0.02	11.79 ± 0.03	7.4 ± 0.2	0.015 ± 0.002	0.064 ± 0.002	48.3 ± 1.7	0.24	0.66	0.62
38	7.23 0.03	12.54 0.03	24.7 0.8	−0.035 0.005	0.161 0.006	76.2 1.3	0.19	0.62	0.82
39	7.29 0.02	12.31 0.03	5.9 0.4	−0.071 0.002	0.129 0.003	46.3 0.5	0.00	0.19	0.31
40	8.29 0.02	11.71 0.02	−3.1 0.2	−0.014 0.001	0.051 0.002	124.3 1.2	0.30	−0.78	−0.66
41	7.76 ± 0.02	11.96 ± 0.02	12.7 ± 0.2	−0.069 ± 0.002	0.025 ± 0.002	33.9 ± 0.9	0.29	0.73	0.71
42	8.17 0.02	12.11 0.02	2.5 0.1	−0.024 0.001	0.014 0.002	82.0 1.1	0.04	0.28	0.25
43	7.98 0.02	12.43 0.02	4.4 0.2	−0.004 0.001	0.016 0.002	105.9 2.4	−0.14	0.41	0.28
44	7.27 0.02	12.42 0.02	7.2 0.2	−0.082 0.002	0.005 0.001	55.3 0.7	0.17	0.48	0.55

simultaneous computation of the average displacement per unit of time of the involved sites, facilitating the introduction of absolute horizontal velocities into the analysis, resulting in a weighted estimation of the absolute average velocity of those sites. A brief description of the deformation quantities, the used parametrization and the formal error propagation scheme are given in Appendix A.

In a first step of the deformation modelling the regional GPS network was divided in 44 triangles as shown in Fig. 4. In each of these triangles an independent set of deformation parameters, including strain rate principal components, was computed (Table 5). This computation requires, for each triangle, the definition of a local topocentric system with origin in the average position of the three involved sites. The absolute horizontal velocities of each vertex were computed applying the associated global-to-topocentric transformation matrices to the (x, y, z)-velocities. Although within each triangle variance–covariance matrix propagation from the (x, y, z)-velocities towards the deformation rate parameters was formally carried out, intertriangle parameter cross-correlations were not computed.

For the definition of the triangles, highly constrained by the distribution of the sites, we have taken into account the traces of the identified faults (according to Menichetti *et al.* 2008). The area of the defined triangles varies between 36 and 660 km^2, with an average value of 284. Along the main trace of the MFFS, due the

higher site density, the triangle average area drops to 85 km^2, providing a better resolution exactly in the zone where strong deformation rate gradients are expected.

In each defined triangle the three pairs of absolute horizontal velocities were transformed, applying eq. (A.15), to six parameters: an average horizontal velocity ($\bar{v}_e$, $\bar{v}_n$), a rigid angular velocity ω around the vertical axis and three strain rate components ϵ_e, ϵ_n and ϵ_{en}. Using eq. (A.11)–(A.13) these representations of the strain rate tensors, aligned to local $\{e, n\}$-topocentric systems, were diagonalized, resulting in strain rate principal components λ_1 and λ_2 and its angle of orientation α_1 (azimuth NESW of λ_1, $\alpha_1 = 90^\circ - \alpha$). In addition, the strain rate second invariants λ were computed applying eq. (A.6) to each triangle.

Although a homogeneous strain rate field was modelled within the limits of each triangle, in Fig. 5 (and following) the computed λ values were interpolated over the entire set of triangles. This did not aim to model the deformation rate with higher resolution, but should help to visualize the deformation patterns, considering that the actual deformation rate field should change continuously over the area regardless of the triangle limits.

The computed strain rate principal components are shown in Fig. 5, superimposed to the interpolated strain rate second invariants. As expected, the strongest deformation activity is concentrated along the main trace of the MFFS, forming an, approximately 30 km wide, longitudinal belt along the 54.6° S parallel. Within this belt a maximum strain rate second invariant of 0.253 ± 0.004 μstrain per year was observed (2σ, 95 per cent confidence; 1 μstrain ≡ 1 mm km^{-1}), slightly to the east of the centre of Fagnano Lake (triangle 35 in Fig. 4). For the zones to the north and south of the deformation belt deformation rates at least one order of magnitude

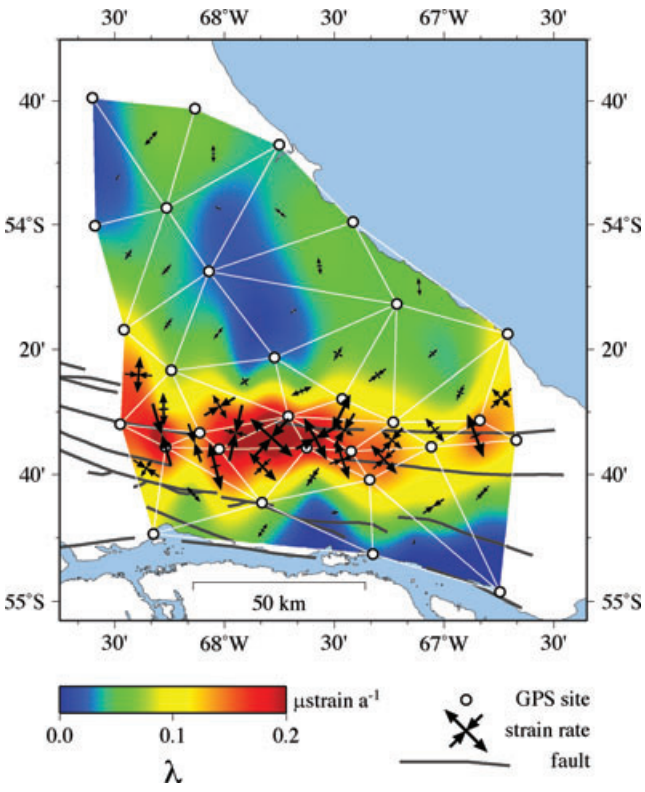

Figure 5. The strain rate principal components for each triangle plotted as vectors of stretching or shortening. The corresponding strain rate second invariants were interpolated and plotted in the background.

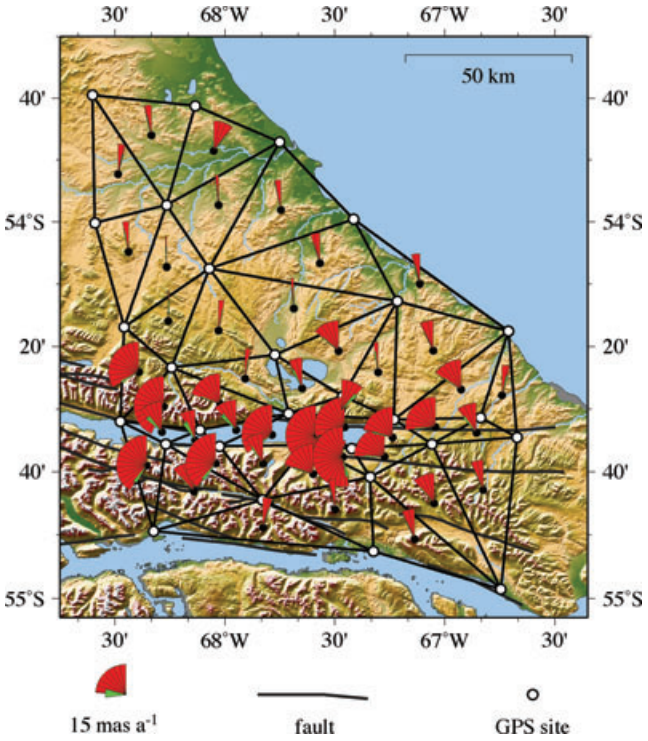

Figure 6. Computed rotation rates plotted as unfolded wedges with origin in each triangle average position. Each unfolded quadrant represents a rotation rate of 15 mas a^{-1}.

weaker than within the belt, but still significant (e.g. triangles 3 and 4), were detected.

The computed angular velocities for each triangle are shown in Fig. 6, where almost all the rotation rates are positives, in excellent agreement with the left-lateral sense of the MFFS. Although within each triangle the used parametrization accounts for rigid rotational displacements, the differential rotation rates between adjacent triangles represent actual deformation. This deformation component, at a scale slightly larger than the triangles, extends in a belt following the same spatial pattern of the strain rate. Nevertheless, the rotation rates present a local minimum inside this deformation belt, right at the centre of Fagnano Lake (triangles 32, 33 and 34). The maximum rate corresponds to the triangle 22, where 45.5 ± 0.8 mas a^{-1} was obtained (2σ, 95 per cent confidence), and coincides approximately with the area where the strain rate maximum was detected.

3.2 Separation of the strain rate principal components

The computed regional strain rate field could be modelled as the superposition of two linearly independent fields, representing components of shortening and stretching of the crust. These two separated components, based on the sign of each eigenvalue, are shown in Fig. 7 (stretching) and Fig. 8 (shortening). Here, a clear change in deformation style along the belt becomes evident: predominant shortening of the crust to the west, near the centre of Fagnano Lake, and significant stretching on the east.

The orientation of the extensional components, shown in Fig. 7, is in good agreement with the left lateral style of the MFFS. In particular, our results support the present-day transtensional regime for the fault system in this area reported by Tassone *et al.* (2005) based on geomagnetic data profiles near the western shore of Fagnano Lake.

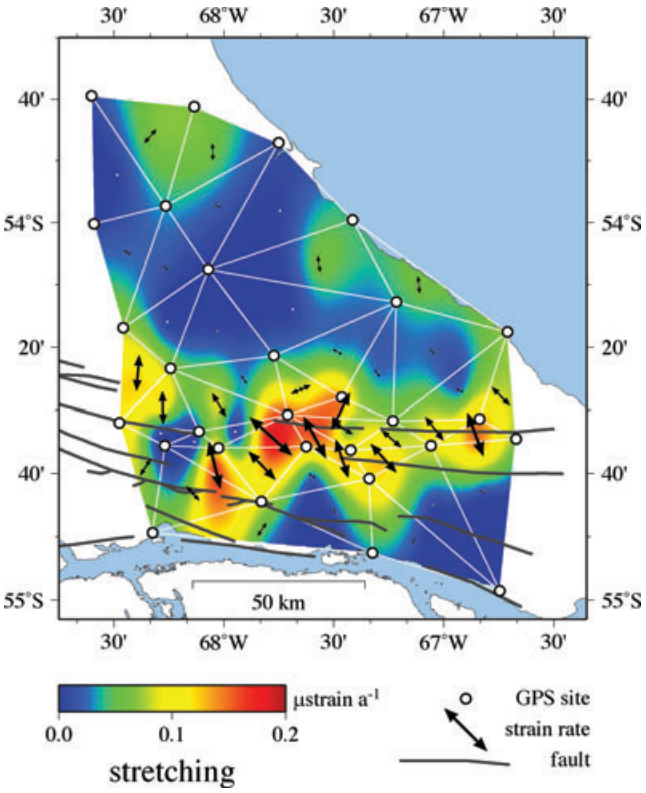

Figure 7. Positive strain rate principal components, representing stretching of the triangles, are plotted and interpolated in the background.

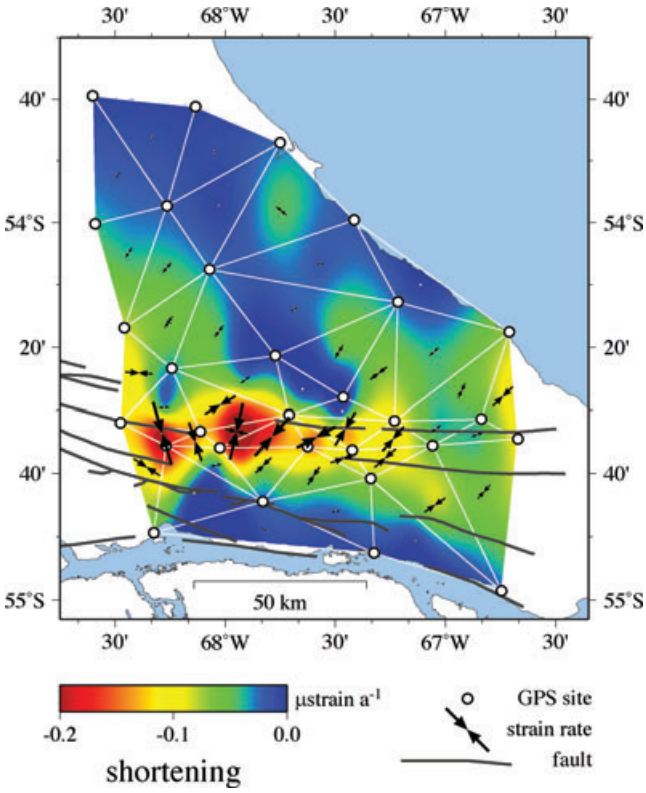

Figure 8. Negative strain rate principal components, representing shortening of the triangles, are plotted and interpolated in the background.

On the other hand, the average orientation of the shortening components is in N–S direction, contrasting with the E-W orientation of the faults' traces (triangles 32, 33 and 34). This area coincides with the set of triangles inside the deformation belt for which a local minimum of rotation rates was observed. A change of regime seems to occur near 67° 50′W (triangle 35) where the extensional pattern splits into two branches to the south (the main) and to the north of the lake.

3.3 Quantification of SA–SC plates relative movement across the MFFS in TDF

A direct comparison of individual site velocities may not provide a useful quantification of the movement accommodated across the SA–SC boundary in TDF. These relative velocities are clearly site-dependent and are affected by residual local effects. A more reliable estimate can be obtained from the comparison of averaged absolute velocities over two sets of specifically chosen sites, to either sides of the boundary, provided that within each set the deformation is small. The (geodynamically) less active zones identified at both sides of the deformation belt, indicated as shadowed areas in Fig. 9, provide these sets of sites.

For both zones strain, rotation and displacement rates were estimated simultaneously by means of a least squares adjustment, including the formal propagation of the full variance–covariance matrix of the velocities to the estimated parameters (Table 6). The strain and rotation rate parameters take into account any residual deformation, and confirm the initial assumption of the relative rigidity of both zones (within its formal uncertainties). The difference of absolute displacement rates between both zones, 4.4 ± 1.1 and -0.3 ± 0.8 mm a^{-1} in east and north directions, respectively (2σ, 95 per cent confidence), constitutes an estimation of the relative movement accommodated across the MFFS in the island.

This result is in excellent agreement with the velocity estimated by Del Cogliano *et al.* (2000), who also did not include sites located within the deformation belt.

3.4 Horizontal strain rate and relative uplift

An important result was obtained by the comparison of the horizontal strain rate field and the vertical velocities near the main trace of the MFFS. In this area, and since the network densification performed in 2003, a highly reliable subset of vertical velocities is available, due to the use of GPS antennas mounted exclusively by forced centring (on concrete pillars or bedrock) and also due to the longer times of continuous observation per campaign (several days, Table 1). As a consequence, it was possible to obtain a joint picture of the present-day horizontal and vertical deformation rates along this segment of the MFFS.

A relative uplift of 3.1 ± 0.4 mm a^{-1} (2σ, 95 per cent confidence) was estimated for the area located at west of 67° 50′W with respect to the eastern sites (Fig. 10). This result follows from the mean absolute vertical velocities of western and eastern sites: 3.3 ± 0.3 and 0.2 ± 0.2 mm a^{-1}, respectively (western sites: PISA, TORI, ESPE, PALA, eastern sites: RIOS, PRE2, EUSH, EOLO, ESCO, ESSA, IRIS).

The observed uplift is not only significant within its formal uncertainty, it presents also the same spatial pattern revealed by the horizontal extension and contraction rates. The western area, where the uplift is observed, coincides with the area where the maximum of shortening and the minimum of stretching were detected by the strain rate analysis (triangles 32, 33 and 34). It is clear that

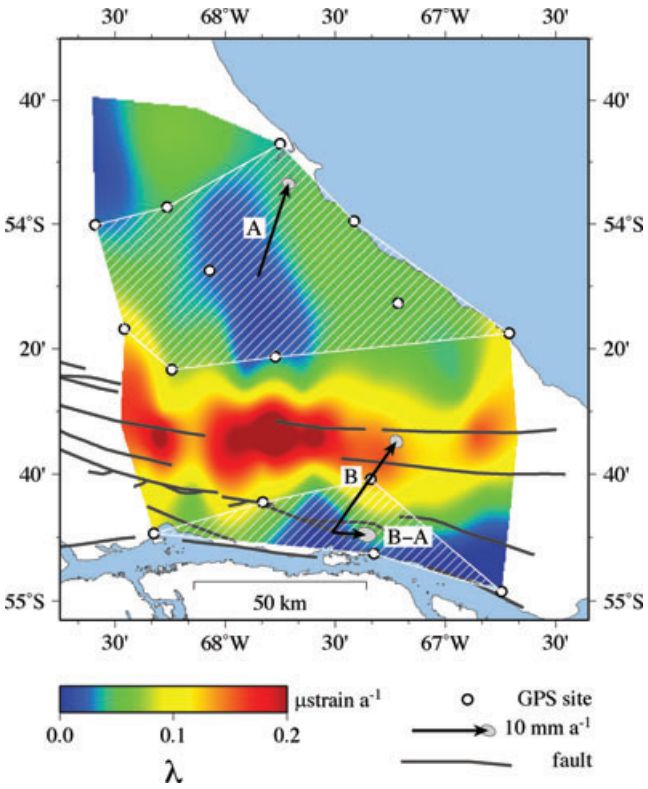

Figure 9. In order to quantify the relative movement accommodated across the MFFS, in the island, the difference in mean yearly displacement between both less active zones was estimated (Table 6).

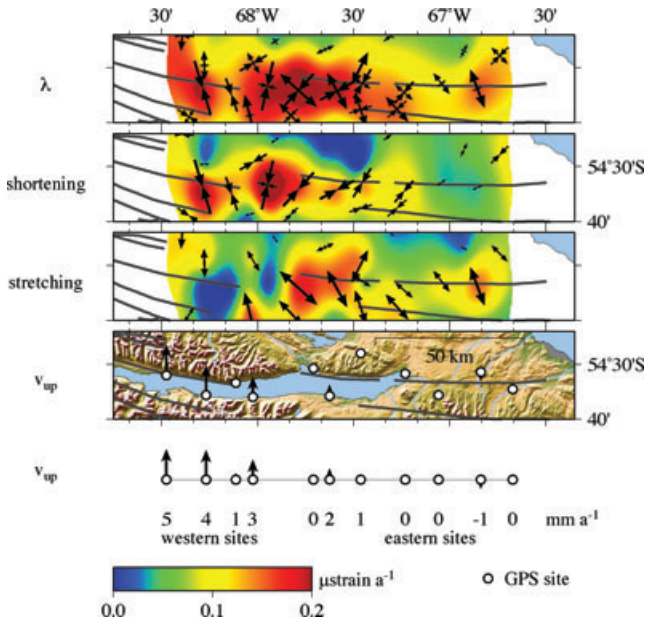

Figure 10. Spatial correlation between horizontal and vertical deformation rates was observed. In the bottom, a profile shows the absolute vertical velocities of each GPS site; the numbers represent the numerical value of the velocities rounded to 1 mm a^{-1}.

the cross-correlations between the estimated horizontal and vertical velocities can not explain this result. While significant neotectonic uplift could be responsible for this signal, the effects of glacial isostatic adjustment processes in the area (Ivins & James 2004) should be considered in addition.

4 CONCLUSIONS

The analysis of more than a decade of GPS data has resulted in the materialization of a dense and reliable reference frame in the TDF island. Its associated field of velocities provide valuable information about the present-day relative movement across the SA–SC boundary in this region.

The observed horizontal deformation accommodates across a 30-km-wide belt, surrounded by less active areas, and is clearly aligned with the identified traces of the MFFS and the Fagnano Lake basin. Throughout the interval covered by observations the detected displacements and deformations occur linearly with time.

Within the deformation belt the principal strain components show mainly extension of the crust, oriented in NW–SE directions, starting south of the lake and ending near the shore of the Atlantic Ocean. Both orientation and magnitude of the deformation along the belt are as expected for an E–W oriented left-lateral transform boundary, and the slow movement accommodated through it. Nevertheless, significant shortening is observed near the centre of the lake, with principal components oriented almost orthogonally with respect to the tectonic boundary. Both results suggest that a transtensional regime, although representative for most of the segment of the MFFS included in our analysis, could not describe accurately the present-day deformation observed near the centre of the Fagnano Lake basin.

The spatial correlation between horizontal and vertical deformation suggests that the uplift observed for the sites near the centre of the Fagnano Lake could be attributed to neotectonics but additional observations and analysis are required to test this assumption, and to quantify the possible contribution of other phenomena including regional glacial isostatic adjustment processes.

ACKNOWLEDGMENTS

The presented research forms part of a bilateral scientific cooperation project of Universidad Nacional de La Plata, Facultad de Ciencias Astronómicas y Geofísicas and Technische Universität Dresden, Institut für Planetare Geodäsie, funded by SECyT, Argentine and the IB des BMBF, Germany (Project No. AL/PA01-UV II/01).

Table 6. Estimated displacement, rotation and strain rate parameters for the least active zones (shadowed areas in Fig. 9), including their formal errors (2σ, 95 per cent confidence) and the *a posteriori* standard deviation of the unit of weight σ_1; the relative velocity of the zone B with respect to the zone A is also shown.

Zone	Sites	$\overline{v}_e$ (mm a^{-1})	$\overline{v}_n$ (mm a^{-1})	ω (mas a^{-1})	λ_1 (μstrain a^{-1})	λ_2 (μstrain a^{-1})	α_1 ° (NESW)	σ (mm a^{-1})
A	10	3.7 ± 0.8	12.4 ± 0.6	−0.05 ± 1.46	−0.014 ± 0.011	0.002 ± 0.010	53.9 ± 28.5	0.9
B	5	8.1 0.8	12.1 0.6	2.58 3.46	−0.006 0.012	0.008 0.042	99.8 71.5	0.8
B−A		4.4 ± 1.1	−0.3 ± 0.8					

The Deutscher Akademischer Austausch Dienst (DAAD, Germany) and the Ministerio de Educación (ME, Argentina) have collaborated by means of a research scholarship.

Furthermore we would like to thank Gerardo Connon, Luis Barbero and Carlos Ferrer from EARG; M. Eugenia Gomez and Diego Bagú from FCAG-UNLP; Gunter Reppchen from HTW Dresden; family Echeverria from Bahía El Torito, Fagnano Lake; Tommy and Nathalie Goodal from Estancia Harberton, Beagle Channel; and Prefectura Naval Argentina, Destacamento Lago Fagnano, for operational support of the field work.

All the maps and plots were generated with the GMT software (Wessel & Smith 1995).

REFERENCES

Barker, P.F., 2001. Scotia Sea regional tectonic evolution: implications for mantle flow and paleocirculation, *Earth Sci. Rev.,* **55,** 1–39.

Beutler, G. *et al.*, 2007. *Bernese GPS Software Version 5.0,* eds Dach, R., Hugentobler, U., Fridez, P. & Meindl, M., Astronomical Institute, University of Bern.

Bibby, H.M., 1982. Unbiased estimate of strain from triangulation data using the method of simultaneous reduction, *Tectonophysics,* **82,** 161–174.

Bird, P., 2003. An updated digital model of plate boundaries, *Geochem. Geophys. Geosyst.,* **4**(3), doi:10.1029/2001GC000252.

Buffoni, C., Sabbione, N.C., Connon, G. & Hormaechea, J.L., 2009. Localización de hipocentros y determinación de su magnitud en Tierra del Fuego y zonas aledañas, *Geoacta,* **34,** 75–85.

Cunningham, W.D., Dalziel, I.W.D., Lee, T.-Y. & Lawver, L.A., 1995. Southern South America-Antartic Peninsula relative plate motions since 84 Ma: implications for tectonic evolution of the Scotia Arc region, *J. Geophys. Res.,* **100**(B5), 8257–8266.

Del Cogliano, D., Perdomo, R., Hormaechea, J.L., Olivero, E., Strelin, J. & Martinioni, D., 2000. GPS detection of movements between SCO and SAM plates in the Argentinean part of Tierra del Fuego Island, in *31st International Geological Congress,* Rio de Janeiro, Brazil.

Dietrich, R., Ivins, E.R., Casassa, G., Lange, H., Wendt, J. & Fritsche, M., 2009. Rapid crustal uplift in Patagonia due to enhanced ice loss, *Earth planet Sci. Lett.*, doi:10.1016/j.epsl.2009.10.021.

Drewes, H., 2009. The actual plate kinematic and crustal deformation model APKIM2005 as basis for a non-rotating ITRF, in *Geodetic Reference Frames,* pp. 95–99, eds Sansò, F. & Drewes, H., Springer, Berlin.

Ferland, R., 2006. [IGSMAIL-5455]: IGS05 Fine Tuning, igscb.jpl.nasa.gov/mail/igsmail/2006/msg00178.html (last accessed 2006 November 3).

Fritsche, M., Dietrich, R., Knöfel, C., Rülke, A., Vey, S., Rothacher, M. & Steigenberger, P., 2005. Impact of higher–order ionospheric terms on GPS estimates, *Geophys. Res. Lett.,* **32**(23), doi:10.1029/2005GL024342.

Ivins, E.R. & James, T.S., 2004. Bedrock response to Llanquihue Holocene and present-day glaciation in southernmost South America, *Geophys. Res. Lett.,* **31,** L24613, doi:10.1029/2004GL021500.

Jaschek, E., Sabbione, N. & Sierra, P., 1982. *Reubicación de sismos localizados en territorio argentino (1920–1963),* Vol. XI of Geofísica, Publicaciones Observatorio de la Universidad Nacional de La Plata.

Lodolo, E., Menichetti, M., Bartole, R., Ben-Avraham, Z., Tassone, A. & Lippai, H., 2003. Magallanes-Fagnano continental transform fault (Tierra del Fuego, southernmost South America), *Tectonics,* **22**(6), doi:10.1029/2003TC001500.

Lomnitz, C., 1970. Major earthquakes and tsunamis in Chile, *Geologische Rundschau,* **59**(951), doi:10.1007/BF02042278.

McCarthy, D. and Petit, G. (eds), 2004. IERS Conventions (2003), IERS Technical Note No. 32, IERS Conventions Centre.

Menichetti, M., Lodolo, E. & Tassone, A., 2008. Structural geology of the Fuegian Andes and Magallanes fold-and-thrust belt—Tierra del Fuego Island, *Geol. Acta,* **6**(1), 19–42.

Michel, V. & Person, T., 2003. From geodetic monitoring to deformation tensors and their reliability, in *11 FIG Symposium on Deformation Mesurements Proceedings Volume,* eds Stiros, S.C. & Pytharouli, S., Patras University.

Olivero, E.B. & Martinioni, D.R., 2001. A review of the geology of the Argentinian Fuegian Andes, *J. S. Am. Earth. Sci.,* **14,** 175–188.

Pelayo, A.M. & Wiens, D.A., 1989. Seismotectonics and relative plate motion in the Scotia See region, *J. geophys. Res.,* **94**(86), 7293–7320.

Pietrantonio, G. & Riguzzi, F., 2004. Three–dimensional strain tensor estimation by GPS observations: methodological aspects and geophysical applications, *J. Geodyn.,* **38,** 1–18.

Rodríguez, E., Morris, C.S., Belz, J.E., Chapin, E.C., Martin, J.M., Daffer, W. & Hensley, S., 2005. An Assessment of the SRTM Topographic Products, Technical report, JPL, NASA, Jet Propulsion Laboratory D–31639.

Rothacher, M., Shaer, S., Mervart, L. & Beutler, G., 1995. Determination of antenna phase center variations using GPS data, in *Proceedings of the IGS Workshop: Special Topics and New Directions,* pp. 205–220.

Rülke, A., Dietrich, R., Fritsche, M., Rothacher, M. & Steigenberger, P., 2008. Realization of the Terrestrial Reference System by a reprocessed global GPS network, *J. geophys. Res.,* **112,** doi:10.1029/2007JB005231.

Schmid, R., Steigenberger, P., Gendt, G., Ge, M. & Rothacher, M., 2007. Generation of a consistent absolute phase center correction model for GPS receiver and satellite antennas, *J. Geod.,* **81,** 781–798, doi:10.1007/s00190-007-0148-y.

Smalley, R. *et al.*, 2003. Geodetic determination of relative plate motion and crustal deformation across the Scotia-South America plate boundary in eastern Tierra del Fuego, *Geochem. Geophys. Geosyst.,* **4**(9), doi:10.1029/2002GC000446.

Steigenberger, P., Rothacher, M., Dietrich, R., Fritsche, M., Rülke, A. & Vey, S., 2006. Reprocessing of a global GPS network, *J. geophys. Res.,* **111,** doi:10.1029/2005JB003747.

Steigenberger, P., Rothacher, M., Fritsche, M., Rülke, A. & Dietrich, R., 2008. Quality of reprocessed GPS satellillite orbits, *J. Geod.,* **83,** 241–248, doi:10.1007/s00190-008-0228-7.

Tassone, A., Lippai, H., Lodolo, E., Menichetti, M., Comba, A., Hormaechea, J.L. & Vilas, J.F., 2005. A geological and geophysical crustal section across the Magallanes–Fagnano fault in Tierra del Fuego, *J. S. Am. Earth Sci.,* **19,** 99–109.

Wessel, P. & Smith, W.H.F., 1995. New version of the generic mapping tools released, American Geophysical Union, http://www.agu.org/eos_elec.

Willemann, R.J. & Storchak, D.A., 2001. Data collection at the international seismological centre, *Seismol. Res. Lett.,* **72,** 440–453.

Williams, S.D.P., 2003. The effect of coloured noise on the uncertainties of rates estimated from geodetic time series, *J. Geod.,* (76), 483–494.

Williams, S.D.P., Bock, Y., Fang, P., Jamason, P., Nikolaidis, R.M., Prawirodirdjo, L., Miller, M. & Johnson, D.J., 2004. Error analysis of continuous GPS position time series, *J. geophys. Res.,* **109,** doi:10.1029/2003JB002747.

Zhang, J., Bock, Y., Johnson, H., Fang, P., Williams, S., Genrich, J., Wdowinski, S. & Behr, J., 1997. Southern California Permanent GPS Geodetic Array: error analysis of daily position estimates and site velocities, *J. geophys. Res.,* **102**(B8), 18 035–18 055.

APPENDIX A: DEFORMATION MODELING

A1 Continuous deformation field definition

Given a continuous 2-D field of displacements (d_x, d_y) the deformation tensor $\boldsymbol{D}$ is defined by (from Michel & Person 2003)

$$\boldsymbol{D} = \begin{pmatrix} \frac{\partial d_x}{\partial x} & \frac{\partial d_x}{\partial y} \\ \frac{\partial d_y}{\partial x} & \frac{\partial d_y}{\partial y} \end{pmatrix} \tag{A1}$$

For very small displacements this tensor can be expressed as the superposition of symmetric and antisymmetric components

$$\boldsymbol{D} = \underbrace{\begin{pmatrix} \eta + \gamma_1 & \gamma_2 \\ \gamma_2 & \eta - \gamma_1 \end{pmatrix}}_{\boldsymbol{S}} + \underbrace{\begin{pmatrix} 0 & -\omega \\ \omega & 0 \end{pmatrix}}_{\boldsymbol{R}} \tag{A2}$$

where $\boldsymbol{S}$ and $\boldsymbol{R}$ represent a strain tensor and an active rotation matrix, respectively. The dilatation η, the shears γ_1 and γ_2 and the small angle ω characterize the deformation field at every point.

The diagonalization of $\boldsymbol{S}$ provides an alternative and convenient representation of the strain tensor by means of its eigenvalues λ_1 and λ_2, also called principal strain components, and the angle α (orientation of λ_1's eigenvector)

$$\lambda_1 = \eta - \sqrt{\gamma_1^2 + \gamma_2^2} \tag{A3}$$

$$\lambda_2 = \eta + \sqrt{\gamma_1^2 + \gamma_2^2} \tag{A4}$$

$$\alpha = \begin{cases} \arctan\left(\frac{-\gamma_1 - \sqrt{\gamma_1^2+\gamma_2^2}}{\gamma_2}\right) & \text{if } \gamma_2 \neq 0 \\ 0 & \text{if } \gamma_2 = 0 \wedge \gamma_1 < 0 \\ \frac{\pi}{2} & \text{if } \gamma_2 = 0 \wedge \gamma_1 > 0 \\ \text{not defined} & \text{if } \gamma_2 = 0 \wedge \gamma_1 = 0 \end{cases} \tag{A5}$$

While the dilatation η represents an invariant of $\boldsymbol{S}$ with respect to changes of representation, a second invariant is commonly defined as

$$\lambda = \sqrt{\lambda_1^2 + \lambda_2^2} \tag{A6}$$

A2 Discrete deformation rate field computation

Given a discrete 2-D field of velocities (v_{x_i}, v_{y_i}) with $i = 1, \ldots, n$, and under the hypothesis of a homogeneous deformation rate, average deformation rate parameters can be computed from (modified version of the expression given by Pietrantonio & Riguzzi 2004)

$$\underbrace{\begin{pmatrix} v_{x_1} \\ v_{y_1} \\ \vdots \\ v_{x_i} \\ v_{y_i} \\ \vdots \\ v_{x_n} \\ v_{y_n} \end{pmatrix}}_{\mathbf{d}} = \underbrace{\begin{pmatrix} 1 & 0 & x_1 & 0 & y_1 & -y_1 \\ 0 & 1 & 0 & y_1 & x_1 & x_1 \\ \vdots & \vdots & \vdots & \vdots & \vdots & \vdots \\ 1 & 0 & x_i & 0 & y_i & -y_i \\ 0 & 1 & 0 & y_i & x_i & x_i \\ \vdots & \vdots & \vdots & \vdots & \vdots & \vdots \\ 1 & 0 & x_n & 0 & y_n & -y_n \\ 0 & 1 & 0 & y_n & x_n & x_n \end{pmatrix}}_{\boldsymbol{A}} \underbrace{\begin{pmatrix} \overline{v}_x \\ \overline{v}_y \\ \epsilon_x \\ \epsilon_y \\ \epsilon_{xy} \\ \omega \end{pmatrix}}_{\mathbf{u}} \tag{A7}$$

assuming that $(\overline{x}, \overline{y}) = (0, 0)$ (position's origin at the barycenter).

In Eq. A.7 the vector $(\bar{v}_x, \bar{v}_y)$ and the scalar ω represent the average displacement and rotation, per unit of time, of the area occupied by the points (x_i, y_i) as a whole rigid block. The homogeneous deformation rate is therefore accounted exclusively by the quantities ϵ_x, ϵ_y and ϵ_{xy}, which are related to the strain rate parameters by

$$\eta = \frac{\epsilon_x + \epsilon_y}{2} \tag{A8}$$

$$\gamma_1 = \frac{\epsilon_x - \epsilon_y}{2} \tag{A9}$$

$$\gamma_2 = \epsilon_{xy} \tag{A10}$$

The diagonalized strain rate parameters result

$$\lambda_1 = \frac{\epsilon_x + \epsilon_y - \Delta}{2} \tag{A11}$$

$$\lambda_2 = \frac{\epsilon_x + \epsilon_y + \Delta}{2} \tag{A12}$$

$$\alpha = \begin{cases} \arctan\left(\frac{\epsilon_y - \epsilon_x - \Delta}{2\epsilon_{xy}}\right) & \text{if } \epsilon_{xy} \neq 0 \\ 0 & \text{if } \epsilon_{xy} = 0 \wedge \epsilon_x < \epsilon_y \\ \frac{\pi}{2} & \text{if } \epsilon_{xy} = 0 \wedge \epsilon_x > \epsilon_y \\ \text{not defined} & \text{if } \epsilon_{xy} = 0 \wedge \epsilon_x = \epsilon_y \end{cases} \tag{A13}$$

with

$$\Delta = \sqrt{\epsilon_x^2 - 2\epsilon_x\epsilon_y + \epsilon_y^2 + 4\epsilon_{xy}^2} \tag{A14}$$

Eq. A.7 requires $n \geq 3$. In the case $n = 3$ the matrix $\boldsymbol{A}$ becomes a linear transformation, between both vectors $\mathbf{d}$ and $\mathbf{u}$, and the parameters can be directly calculated by

$$\mathbf{u} = \boldsymbol{A}^{-1}\mathbf{d} \tag{A15}$$

If $n > 3$ $\boldsymbol{A}$ becomes a design matrix. In this case, and provided a weight matrix

$$\boldsymbol{P_d} \approx \sigma_0^2 \boldsymbol{C_d}^{-1} \tag{A16}$$

where σ_0^2 and $\boldsymbol{C_d}$ are the a priori variance of the unit of weight and the full variance-covariance matrix of the observation vector $\mathbf{d}$, the parameters can be estimated by a weighted least squares adjustment

$$\mathbf{u} = \left(\boldsymbol{A}^{\mathrm{T}} \boldsymbol{P_d} \boldsymbol{A}\right)^{-1} \boldsymbol{A}^{\mathrm{T}} \boldsymbol{P_d} \mathbf{d} \tag{A17}$$

In both cases the full variance-covariance matrix of the parameters vector $\mathbf{u}$ can be obtained by

$$\boldsymbol{C_u} = \begin{cases} \boldsymbol{A}^{-1} \boldsymbol{C_d} \left(\boldsymbol{A}^{-1}\right)^{\mathrm{T}} & \text{if } n = 3 \\ \sigma^2 \left(\boldsymbol{A}^{\mathrm{T}} \boldsymbol{P_d} \boldsymbol{A}\right)^{-1} & \text{if } n > 3 \end{cases} \tag{A18}$$

where σ^2 represents the *a posteriori* variance of the unit of weight computed with the residuals of the adjustment. The variance-covariance matrices associated to the strain rate parameters and to the average displacement and rotation per unit of time, $\boldsymbol{C_s}$, $\boldsymbol{C_v}$ and σ_ω^2 respectively, could be directly obtained as submatrices of $\boldsymbol{C_u}$.

Given $\boldsymbol{C_s}$, the variance-covariance matrix of the strain rate parameters η, γ_1 and γ_2 results

$$\boldsymbol{C}_{\eta\gamma_1\gamma_2} = \boldsymbol{F}_1 \boldsymbol{C_s} \boldsymbol{F}_1^{\mathrm{T}} \tag{A19}$$

with

$$\boldsymbol{F}_1 = \begin{pmatrix} \frac{1}{2} & \frac{1}{2} & 0 \\ \frac{1}{2} & -\frac{1}{2} & 0 \\ 0 & 0 & 1 \end{pmatrix} \tag{A20}$$

while the variance-covariance matrix of the strain rate principal components λ_1 and λ_2 and the orientation angle α results

$$\boldsymbol{C}_{\lambda_1\lambda_2\alpha} = \boldsymbol{F}_2 \boldsymbol{C_s} \boldsymbol{F}_2^{\mathrm{T}} \tag{A21}$$

with

$$\boldsymbol{F}_2 = \begin{pmatrix} \frac{1}{2} - \frac{\epsilon_x - \epsilon_y}{2\Delta} & \frac{1}{2} + \frac{\epsilon_x - \epsilon_y}{2\Delta} & \frac{-2\epsilon_{xy}}{\Delta} \\ \frac{1}{2} + \frac{\epsilon_x - \epsilon_y}{2\Delta} & \frac{1}{2} - \frac{\epsilon_x - \epsilon_y}{2\Delta} & \frac{2\epsilon_{xy}}{\Delta} \\ -\frac{\epsilon_{xy}}{\Delta^2} & \frac{\epsilon_{xy}}{\Delta^2} & \frac{\epsilon_x - \epsilon_y}{\Delta^2} \end{pmatrix} \tag{A22}$$

if $\epsilon_{xy} \neq 0$ or

$$\boldsymbol{F}_2 = \begin{pmatrix} 1 & 0 & 0 \\ 0 & 1 & 0 \\ 0 & 0 & \frac{1}{\epsilon_x - \epsilon_y} \end{pmatrix} \tag{A23}$$

if $\epsilon_{xy} = 0 \wedge \epsilon_x < \epsilon_y$ or

$$\boldsymbol{F}_2 = \begin{pmatrix} 0 & 1 & 0 \\ 1 & 0 & 0 \\ 0 & 0 & \frac{1}{\epsilon_x - \epsilon_y} \end{pmatrix} \tag{A24}$$

if $\epsilon_{xy} = 0 \wedge \epsilon_x > \epsilon_y$ or

$$\boldsymbol{F}_2 = \begin{pmatrix} 1 & 0 & 0 \\ 0 & 1 & 0 \\ 0 & 0 & \infty \end{pmatrix} \tag{A25}$$

if $\epsilon_{xy} = 0 \wedge \epsilon_x = \epsilon_y$.